ELSEVIER

Contents lists available at ScienceDirect

Cement and Concrete Composites

journal homepage: www.elsevier.com/locate/cemconcomp



Uncover the thermal behavior of geopolymer: insights from in-situ high temperature exposure

Y. Luo^a, K.M. Klima^b, S. Melzer^b, H.J.H. Brouwers^a, Qingliang Yu^{a,*}

ARTICLE INFO

Keywords: Alkali activation Geopolymer High temperature Thermal behavior In-situ Ex-situ

ABSTRACT

The understanding of geopolymers' behavior at elevated temperatures is lacking due to the most focuses on post-situ research, leading to unsubstantiated expectations of in-situ thermal performance. This work systematically investigates the in-situ thermal behavior of geopolymers, including phase changes, deformation, and mechanical performance, following a comparison between in-situ and ex-situ properties. The results reveal a notable discrepancy between the in-situ and ex-situ thermal performance of geopolymers. During heating, geopolymers shift from a brittle to a ductile state by physicochemical transformation, facilitating accommodation of thermal incompatibilities. As we observed, the in-situ mechanical strength and creep strain increase until partial melting, with higher Na₂O% accelerating melting of geopolymer. During cooling, geopolymers undergo matrix shrinkage and cracking, which impairs ex-situ performance. A denser matrix provides superior in-situ strength, while its high stiffness negatively impacts structural integrity during cooling, further reducing residual strength. These findings highlight the limitations of ex-situ experiments in estimating high-temperature performance of geopolymers. To accurately predict the in-situ thermal performance, future ex-situ research must account for partial melting during heating and deterioration induced by cooling.

1. Introduction

Geopolymers are known as promising cementitious materials, specifically yielding a three-dimensional network of aluminate and silicate tetrahedra [1,2]. These binders can be produced by the alkali-activation of aluminosilicate-rich industrial wastes, with Class F fly ash being the most commonly used precursor [3]. The main reason that geopolymers have received much interest from both the academic and industrial communities over the past decade is related to the low CO₂ footprint and reduced energy consumption, in comparison to ordinary Portland cement (OPC)-based materials [4]. In addition, the typical three-dimensional aluminosilicate network of geopolymers contributes to good thermal stability. As compared to OPC, geopolymer exhibits superior structural integrity under elevated temperatures by largely retaining the aluminosilicate gel structure after dehydration [5-8]. In this regard, geopolymers show high potential to serve as a promising alternative to OPC-based materials for construction of high-fire-risk infrastructure, e.g., tunnels, underground structures, and high-rise buildings, etc. However, the thermal behavior of geopolymer varies strongly with raw material composition, alkali type/concentration,

silica modulus, water-to-binder ratio, etc. [9–11]. For this reason, geopolymers are still far from a one-size-fits-all solution for addressing the construction needs of high-fire-risk infrastructures.

Despite the thermal behavior of geopolymers has been extensively investigated, recent studies are mostly focused on residual properties after high temperature exposure [12]. In general, even though geopolymers experience cracking and volumetric deformation at high temperatures, the further geopolymerization before 400 °C as well as the viscous sintering at around 800 °C heal cracks and/or fill pores, enabling matrix densification [13–15]. Consequently, in certain cases, geopolymers exhibit enhanced mechanical strength after exposure to high temperatures, a feature that distinguishes them from OPC-based binders [16]. However, apart from the advantage of high residual strength, it is also reported that during high temperature exposure, geopolymer undergoes abrupt loss of stiffness at around 600 °C, accompanying significant deformation, because of the softening of aluminosilicate glasses [17,18]. The densification and solidification of geopolymers during cooling could obscure the effect of volumetric deformation, cracking, and partial melting during heating. Thus, the insights based on ex-situ thermal behavior provide poor predictions of the high-temperature

a Department of the Built Environment, Eindhoven University of Technology, P.O. Box 513, 5600MB, Eindhoven, the Netherlands

^b Tata Steel Nederland B.V. (Tata Steel Ijmuiden), P.O. Box 10.000, 1970 CA, IJmuiden, the Netherlands

^{*} Corresponding author.

E-mail address: q.yu@bwk.tue.nl (Q. Yu).

performance of geopolymers.

Currently, constrained by the technical complexity of conducting insitu thermal tests, which necessitate specialized high-temperatureresistant apparatus, scarce studies on the in-situ thermal behavior of geopolymers are available. Fernández-Jiménez et al. [19] reported a comparative study of the in-situ mechanical performance between OPC and fly ash based geopolymer, testifying to the superior mechanical performance of geopolymer over OPC both during and after high temperature exposure. Pan et al. [17] investigated the stress-strain behavior of fly ash based geopolymer paste during thermal exposure, and observed that the compressive strength kept increasing from 290 to 520 $^{\circ}\text{C}$ until an abrupt loss of stiffness because of glass transition. As reported by the same authors [20], who conducted a thermal release analysis on geopolymers during heating, the inferred increase in strength before partial melting was ascribed to the continued reaction between fly ash and the alkali activator. More recently, Wang et al. [21] investigated the effect of slag addition on the thermal properties of hybrid geopolymers, with a focus on the strength and elastic modulus evolution at elevated temperatures. It was found that a certain content of slag incorporation further reduces the density loss and promotes the strength gain during the thermal exposure before sudden stiffness loss. Based on the above discussion, the initial properties of geopolymers along with the related phase and microstructural changes that occur under high temperatures, are key factors influencing the in-situ thermal performance of geopolymer-based materials.

In conclusion, characterizing the in-situ evolution of geopolymers is critical for advancing the fundamental understanding of their real-time high-temperature responses. While the majority of studies only focused on hot mechanical properties, scarce studies have verified the in-situ physicochemical evolution of geopolymers [22]. In particular, the interrelationship between physicochemical changes and mechanical performance during exposure remains insufficiently characterized. Furthermore, the reliability of insights obtained from ex-situ testing remains uncertain, and their applicability to time-dependent thermal exposures requires further validation.

In light of aforementioned research gaps, the major aims of this study are to intrinsically characterize the in-situ thermal response of geopolymer binders during high temperature exposure, and subsequently to reveal intercorrelation among the thermal physicochemical properties, and their further impact on mechanical performance during high temperature exposure. To reach these goals, by tailoring alkali concentrations, geopolymers with different polymerization degrees are adopted in this study, differentiated by hydration degree, bulk density, and initial mechanical strength. The in-situ physicochemical properties during high temperature exposure are investigated by thermogravimetric analysis (TGA), high temperature X-ray diffractometry (XRD), FactSage and dilatometry. The identified physicochemical transformations are further correlated to the in-situ mechanical properties and creep behavior. Lastly, a comparative study between the in-situ and ex-situ thermal performance of geopolymers is conducted.

This study innovatively presents the systematic investigation of the in-situ thermal behavior of geopolymers from aspects of phase changes, deformation, and mechanical performance during high temperature exposure. Importantly, the generalizability of previous findings regarding the residual properties is discussed. The in-situ observations enhance fundamental understanding of geopolymer evolution under high temperature exposure, and provide important information for future research targeting more realistic and complex fire conditions. The insights from this study can help guide the future design of geopolymer-based materials for high-temperature and fire-resistant applications.

2. Experimental program

2.1. Materials

Low calcium (Class F) fly ash (FA) was applied to prepare

geopolymer in this study. According to our previous study, an industrial residual from steel manufacturing, ladle furnace slag (LS), was used as a co-precursor to improve the geopolymer performance, such as workability, mechanical strength, and thermal behavior. Commercially available Class F FA was provided by Vliegasunie (The Netherlands) and used directly. LS was collected from stockpiles at Tata Steel (The Netherlands), followed by drying and milling. The dried LS was grounded via a ball mill (FRITSCH, PULVERISETTE 5) for 40 min at 250 rpm before use. Four 500 mL grinding bowls were loaded in the ball mill, and 250 g of LS and 24 steel balls ($\emptyset = 20 \text{ mm}$) were fed into each bowl. The applied FA and treated LS have an average particle size (d50) of 14.08 and 18.91 μm respectively, as determined with laser diffraction particle size analysis, Mastersizer 2000 (Malvern Instruments, UK. The chemical composition based on X-ray fluorescence (XRF, PANalytical Epsilon 3) and loss on ignition (LOI) up to 1000 °C of FA and LS are given in Table 1. A relatively high LOI of 10.18 % is detected in LS, indicating the weathering of slag in the stockpiles. The mineralogical phases of the raw materials are identified by X-ray diffraction (XRD). As shown in Fig. 1, quartz (SiO₂), mullite (Al_{1.69}Si_{1.22}O_{4.85}), hematite (Fe₂O₃), and magnetite (Fe₃O₄) are detected in FA. In terms of LS, calcium aluminates, including mayenite (C₁₂A₇) and tricalcium aluminate (C₂A) are observed as the main anhydrous crystalline phases. Notably, in line with TGA, hydrogarnet (C₃AH₆), portlandite (Ca(OH)₂), and hydrotalcite $((Mg_{0.667}Al_{0.333})(OH)_2(CO_3)_{0.167}(H_2O)_{0.5})$ are noticed owing to the weathering and wet-recovery process of meta. Commercially available sodium hydroxide (NaOH) pellets (analytical level, 99.8 %) and water glass (Na₂SiO₃) solution (27.69 wt% SiO₂, 8.39 wt% Na₂O, and 63.9 wt % H₂O) were used for alkali activator preparation. Deionized water was used to tailor the water-to-binder ratio.

2.2. Mix design and sample preparation

The mix proportions are determined through our prior research focused on optimizing hybrid ladle slag/class F fly ash geopolymers [23, 24]. As shown in Table 2, the blend mass ratio of FA and LS, silica modulus (Ms), and water-to-binder ratio (w/b) are fixed. Two typical Na₂O percentages, namely 6 % and 8 %, were employed to prepare paste samples with different reaction degree, denoted as GP6 and GP8 respectively. Moreover, the compressive strength of GP6 and GP8 at 28 days are compared in Table 2.

The alkali-activator was synthesized 24 h before sample casting, allowing to cool down to room temperature (20 \pm 1 $^{\circ}$ C). Specific amounts of NaOH, water glass, and deionized water were mixed to achieve desired compositions. For the sample preparation, FA and LS powder were blended for 5 min using a Hobart mixer. After the powders reached a homogeneous state, the activator was added while stirring. The slurry was mixed at a low speed for 30 s, followed by another high-speed mixing for 60 s. Afterward, the slurry was poured into plastic molds and sealed with plastic film. The sealed samples were cured at room temperature for 24 h and then cured at 60 $^{\circ}$ C for 24 h. After high temperature curing, the hardened samples were demolded and stored at room temperature under sealed condition.

After 28 days of curing, the samples were processed into cylinders via wet drilling. Cylinders with dimensions $\emptyset=30$ mm, H=50 mm, and $\emptyset=50$ mm, H=50 mm were prepared, and the left-over sample materials were collected. Subsequently, to cease hydration, the collected samples were immersed in Isopropanol for 72 h and then dried at 55 °C for 72 h before further characterization.

2.3. Test methods

2.3.1. Bulk properties (density, porosity, micro-CT)

The bulk density was measured by dividing mass by volume of the samples. The microstructural morphology was characterized by scanning electron microscopy (SEM). A Phenom Pro (The Netherlands) equipped with energy-dispersive spectroscopy (EDS) was applied, and

Table 1
Chemical composition and loss on ignition.

Oxide (wt.%)	SiO_2	Al_2O_3	CaO	Fe_2O_3	MgO	SO_3	K_2O	Others	LOI (1000 °C)
FA	57.07	24.17	4.87	6.68	1.55	0.17	2.13	1.90	1.45
LS	2.58	29.85	49.68	2.54	3.35	0.80	-	1.01	10.18

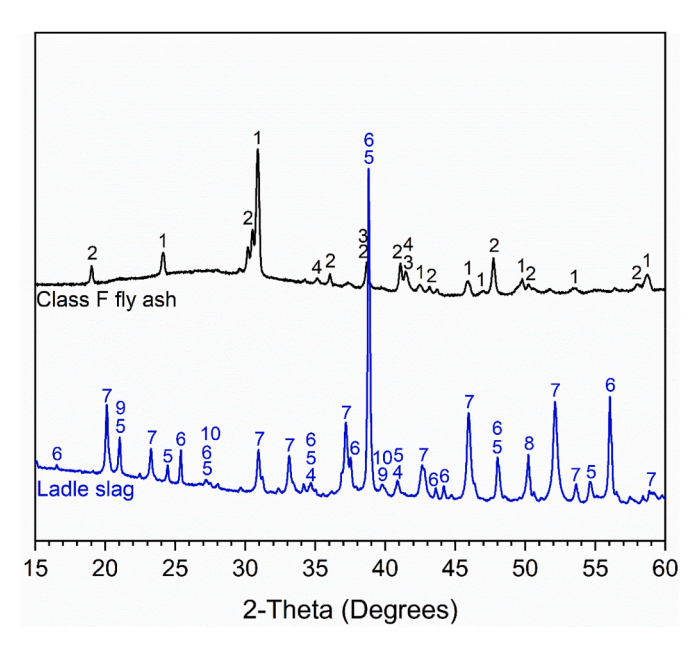


Fig. 1. XRD patterns of raw FA and LS (1-Quartz, 2-Mullite, 3-Hematite, 4-Magnetite, 5-Mayenite, 6-Tricalcium aluminate, 7-Hydrogarnet, 8-Periclase, 9-Portlandite, 10-Hydrotalcite).

Table 2Mix proportions of geopolymers.

Sample code	Mass fract [wt.	ion	Na ₂ O % ^a	Ms ^b	w/ b ^c	Compressive strength ^d [MPa]
	FA	LS				
GP6	85	15	6	1.5	0.35	28.9 (0.8)
GP8	85	15	8	1.5	0.35	37.8 (2.3)

- ^a Equivalent Na percentage in mass.
- $^{\mathrm{b}}$ The mol ratio of SiO_2 to $\mathrm{Na}_2\mathrm{O}$ in alkaline activator.
- ^c The mass ratio of water and binder, in which the water consists of extra deionized water and initial water in the water glass.
- $^{\rm d}$ The compressive strength at the age of 28 days (cylinders, Ø = 30 mm, H = 50 mm).

the investigated samples were cut from the center of the pastes at 28 days. After hydration cessation, the samples were vacuum-impregnated with epoxy resin and polished to obtain a smooth surface. Before observation, the polished samples were coated with Pt using a Quorum 150 TS plus sputter coater under a current of 40 mA. For the testing, an accelerating voltage of 15 kV was applied under a Backscattered electron (BSE) mode. The working distance was between 8 and 10 mm with the magnification of $1000\times$ and $3000\times$.

The pore structure was characterized by applying micro-computed tomography (Micro-CT, Scanco Medical AG, Switzerland). Cylinder samples in size of Ø = 30 mm, and H = 50 mm were used for the test. A fixed X-ray energy (voltage of 70 kV, current of 200 μA) was used. 626 slices were scanned within a thickness of 7.14 mm to calculate and visualize the three-dimensional pore structure with a pixel resolution of 11.4 μm .

2.3.2. In-situ high temperature characterization

In-situ thermal measurements were performed to reveal the heat-induced physico-chemical-mechanical transformations to understand the behavior of geopolymers during thermal exposure. In order to facilitate direct comparison with previously reported ex-situ studies, the thermal exposure settings are designed to investigate the thermal response of geopolymers from a strictly material-focused perspective, following the majority ex-situ studies on geopolymers [5,9,12,16,25].

Thermogravimetry and differential scanning calorimetry (TG-DSC) analysis was carried out with a Jupiter STA 449 F1 Netzsch instrument to learn about the thermal transformation of the samples. Powdered samples (40–60 mg) were loaded and heated up to 1000 $^{\circ}\text{C}$ with a heating rate of 10 $^{\circ}\text{C/min}$, and the measurement was conducted under a Nitrogen atmosphere.

To learn the mineralogical transformation as a function of temperature, high temperature in-situ X-ray diffraction (XRD) was performed using an X'Pert Pro PANalytical diffractometer, equipped with a Co X-ray tube and Anton-Paar HTK2000 heating stage. A thin layer of powder sample was loaded onto a Platinum strip, which serves as the sample holder and serves as strip-heater. The samples were heated up to 700 °C at the rate of 10 °C/min and then cooled to room temperature. A dwelling time of 20 min was employed at intervals of 100 °C for XRD measurements. During the dwelling time, each diffractogram was recorded for 15 min within the range 10–90° 20 using a step size of 0.026° 20.

FactSage software was applied to predict melt (liquid) phase formation under increasing temperatures aided by the Equilibrium Module Gibbs-free energy minimization calculations [26]. The chemical compositions of the samples, as determined by XRF, were modeled using the FToxid and CON4 databases, with a focus on analyzing the melt fraction present at specific temperatures. According to in-situ high temperature XRD analysis, Quartz, mullite, and magnetite were excluded using chemical formulas from ICSD data, due to their inert nature within the matrix during heating. Notably, FactSage is dependent on ideal equilibrium conditions, ignoring kinetic barriers that might inhibit complete phase transformation in alkali-activated materials [27]. Therefore, this study aims to numerically reflect the liquid formation as influenced by thermal diffusion processes occurring within amorphous phases.

The deformation at high temperature was measured with a custom-designed dilatometry according to EN 993-8. Cylinder samples with 50 mm length and 50 mm diameter were used. A preload of $0.02\ \text{N/mm}^2$ was applied to enable the instrument to retain contact with the sample and record the deformation. Additionally, to learn the effect of preload, a load of $0.2\ \text{N/mm}^2$ was performed. Nevertheless, due to the equipment limitation for safety considerations, the measurement with a high preload will be automatically ceased when the deformation reaches 5 %. The measurement temperature was set from 20 to 700 °C with a heating rate of 4 °C/min. A thermal couple was inserted into the centre of the samples to monitor the sample temperature during heating. With the well-controlled heating procedure, one sample was applied for each mixture.

The in-situ high-temperature compressive testing was performed with a custom-made setup. The test apparatus consists of three parts, including a control unit, a radiant tube furnace coupled with the furnace power unit, and a force transducer (Zwick Z250), as presented in Fig. 2. An axis-symmetrical furnace was used for evenly heating the specimen. The heating zone was fully isolated with a cylindrical alumina tube to avoid heat loss and protect the test machine from extreme temperatures. The furnace features openings at both its upper and lower ends, enabling

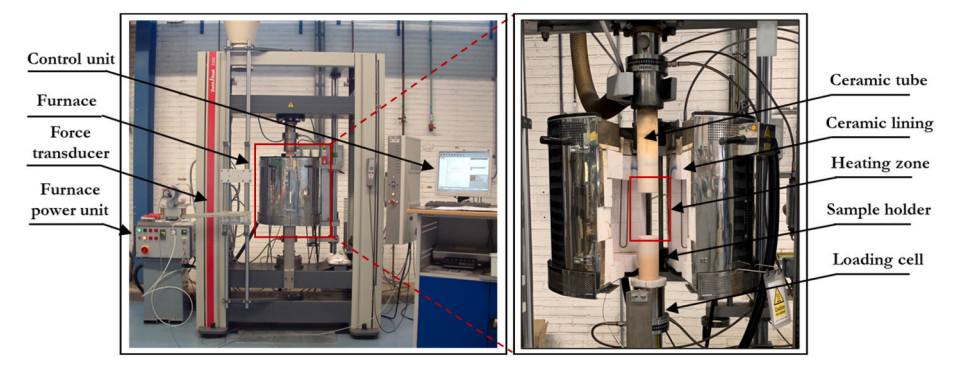


Fig. 2. In-situ compressive test apparatus.

the loading rams to transfer the compressive load from the force transducer to the specimen during heating. The loading rams were extended by using aluminium (99.7 %) tubes to protect the loading rams from direct thermal exposure. The specimens were in the centre of the furnace to ensure uniform heating and encased in an aluminium cover to protect the furnace from sample explosion during crushing.

The testing procedure is illustrated in Fig. 3. The compressive test was performed on cylinders ($\emptyset=30$ mm, H = 50 mm) at 20, 300, 500, and 700 °C. Under the pre-load of 300 N, the samples were heated up to the target temperature at a rate of 5 °C/min and maintained for 1 h to reach thermal equilibrium. Then, force was applied at the rate of 0.05 mm/s at the attained temperature until failure. The stress and strain values were recorded during the testing. The highly controlled heating and uniform heat transfer ensure a high reproducibility of the test. Thus, one sample for each mixture was tested, and the specimen variability was assessed at room temperature (See Table 2).

Due to the high time consumption and experimental costs, one sample from each mixture was used for dilatometry and in-situ high-temperature compressive test, considering the high repeatability of the test. Those in-situ tests show good repeatability with a well-controlled heating program. On the other hand, the variability in in-situ performance can be assessed under both ambient conditions and post-exposure.

2.3.3. Ex-situ characterization

For the investigation of the post-high temperature performance of geopolymers and to compare this with in-situ performance, geopolymers of the same dimensions were applied. An identical heating program as depicted in Fig. 3 was applied using a muffle furnace. Based on the typical thermally induced transitions of geopolymers, i.e., dehydration, further geopolymerization, and glass transition, the target temperatures of 300, 500, and 700 °C were selected for testing. After 1 h of dwelling at the target temperature, the samples were naturally cooled down to room

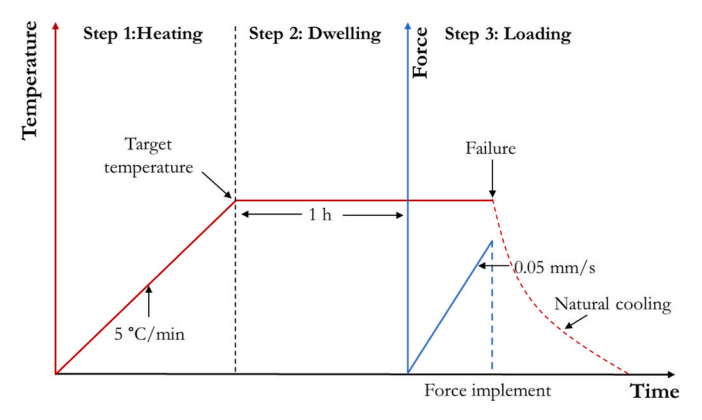


Fig. 3. Testing procedure of in-situ compressive strength.

temperature in the furnace by turning off the power. Afterward, the samples were sealed using plastic foil to avoid moisture immersion until further tests. For different target temperatures, three replicates were applied for each mixture and tested for linear shrinkage and residual strength.

The linear shrinkage induced by high temperature was measured by comparing the length of cylinder samples before and after high temperature exposure. To determine the residual compressive strength, the compressive test was performed on high temperature exposed cylinder samples with the same dimensions as used in in-situ behavior tests. The facility for post-exposure compressive testing was without heating, under identical operating conditions, namely pre-load of 300 N and loading rate of 0.05 mm/s.

3. Results

3.1. In-situ high temperature characteristics

3.1.1. TGA

The TG-DTG curves of geopolymers at 28 days are presented in Fig. 4a. A continuous mass loss up to 1000 °C is observed in GP6 and GP8, representing 9.52 % and 11.27 % respectively. In the DTG curves, the main mass loss peak in the range of 105-300 °C is interpreted to result from the release of bound water from aluminosilicate hydrates, including N-A-S-H and C-A-S-H [24]. The minor DTG peak centered at 300 °C indicates the presence of hydrogarnet (C₃AH₆), which is introduced by LS [28]. A broad hump from 500 to 750 °C is assigned to the decomposition of CaCO₃ polymorphs of various crystallinity [29,30]. Note that the main discrepancy between GP6 and GP8 lies in the DTG peak for hydrated gels. GP8 exhibits an intensified main mass loss peak as compared to GP6, due to the promoted reaction degree with increased aluminosilicate gels. In addition, to determine the temperature induced reactions in the geopolymers, the DSC results are presented in Fig. 4b. The evaporation of bound water from hydrates leads to an endothermic peak at 150 °C. An exothermic reaction is observed between 150 and 530 °C, which is believed to result from the further geopolymerization [20,31]. As the release of water is a gradual process, temperature could be advantageous to trigger the reaction of unreacted precursors, which promotes continued crosslinking of aluminosilicate gels [25]. In agreement with Pan and Sanjayan [17], an obvious endothermic hump is observed initiated from approximately 530 °C, indicating the start of the glass transition. In this case, the Na₂O% poses an insignificant impact on the glass transition temperature, since close to identical characteristic trends are detected in GP6 and GP8.

3.1.2. In-situ high temperature XRD

The initial XRD patterns of GP6 and GP8 are compared in Fig. 5. Identical crystalline assemblages are detected in GP6 and GP8 due to the same raw material constitution. The main phases, including quartz, mullite, and iron oxides (magnetite and hematite) are introduced by FA.

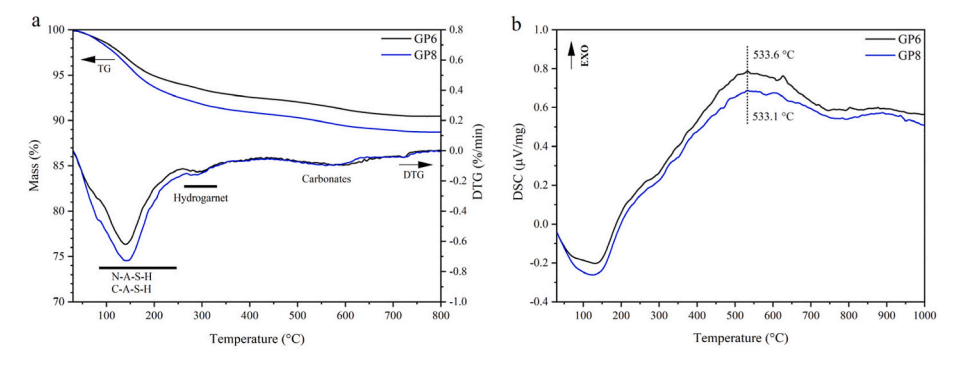


Fig. 4. The TGA-DSC curves of geopolymer pastes.

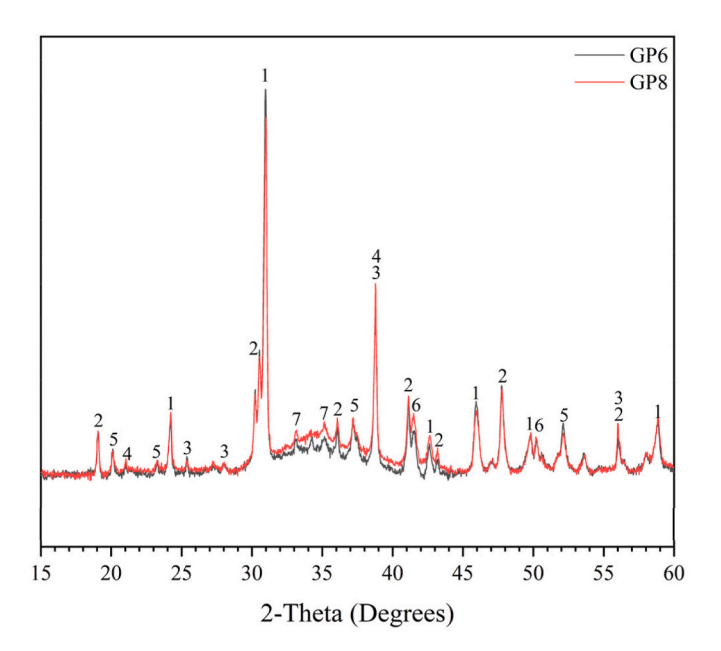


Fig. 5. The XRD patterns of specimens. (1-Quartz, # PDF 01-085-0457, 2-Mullite, # PDF 01-079-1454, 3-Tricalcium aluminate, # PDF 00-006-0495, 4-Mayenite, # PDF 00-048-1882, 5-Hydrogarnet, # PDF 00-024-0217, 6-Iron Oxide, #PDF 01-075-0033, 7-C-(A)-S-H, #PDF 01-083-1242).

The presence of tricalcium aluminate, mayenite, and hydrogarnet reflect the LS contribution. In addition, the amorphous hump between 32 and 35° corresponds to the presence of C-(A)-S-H. Compared to GP6, GP8 shows a lower intensity of calcium aluminates (CAs) and a higher intensity of the amorphous hump. It suggests enhanced dissolution of CAs and increased gel formation in GP8, which is consistent with the TGA results.

To study the crystalline phase variation during heating and cooling, in-situ high temperature XRD is performed on GP6 and GP8, and the XRD patterns at different temperatures are shown in Fig. 6. In general, GP6 and GP8 exhibit similar phase transformations as a function of temperature. Notably, phase changes are observed only during the heating process for both GP6 and GP8, while the crystalline phases remain relatively stable throughout the cooling process. Thus, XRD Rietveld analysis is applied to the heating process, to quantitatively learn the phase transition, the detailed results from XRD-Rietveld are provided in Supplementary material, Table A1.

As shown in Fig. 7, crystalline phases, such as quartz, and mullite, remain almost the same within the investigated temperature range, indicating the thermal stability of those phases. The hydrogarnet decreases with temperature and disappears up to 400 $^{\circ}$ C. This is related to the dehydration and decomposition of hydrogarnet as corroborated by

the TGA results. Correspondingly, there is an intensification in peaks of calcium aluminates, including C_3A and mayenite. There is no recrystallization observed from in-situ XRD, which is in line with previous reports in geopolymers that new phase formation would only appear at higher temperatures than 800 °C [25]. Moreover, in Fig. 6, the peaks of quartz shift to a lower angle during heating and slowly move back to the original position during cooling. The observed transition of peaks is due to the thermal expansion and shrinkage of crystals during heating and cooling, respectively. Herein, a similar mineralogical transformation is detected in GP6 and GP8 at elevated temperatures, while the transformation of crystals during heating and cooling may have a different impact on GP6 and GP8, owing to their varied matrix structure.

At high temperatures, the kinetics of phase transition directly depend on diffusion processes, which are much more prone to take place in amorphous phases than in crystalline ones [32]. In this case, FactSage is used to calculate the liquid formation at high temperatures based on in-situ XRD results, taking both amorphous and crystalline content into consideration. The input data are given in the supplementary materials, Table A2.

In Fig. 8, above 500 °C, GP6 shows the initiation of liquid-phase development (1.3 % melt at 500 °C) while GP8 continues to hold very stable. By 600 °C, the melt starts appearing in both of them, with GP6 with a slightly higher melt fraction (4.6 %) than GP8 (3.0 %). The differences start becoming more significant at around 700 °C. At 700 °C, GP8 has significantly higher melt fractions up to ~ 10 % than GP6 (4.7 %). As the temperature increases further to 800 $^{\circ}$ C, GP8 reaches a melt fraction of 13.5 %, compared to 11.9 % for GP6. Here, alkalis, namely Na₂O lowers the melting point of silicates, facilitating the development of the liquid phase and interfering with the silicate network formation [9,33,34]. Moreover, Fe₂O₃ is present in both materials in nearly similar quantities, and it is likely to favor the liquid formation at higher temperatures, particularly in alkali-rich compositions including GP8, thereby encouraging shrinkage [35]. With increasing temperature, the viscosity of the melt phase decreases, hence pores collapse, and shrinkage are initiated [36]. Those phenomena will be discussed in the following sections.

3.1.3. Dilatometry

The linear dimensional change of GP6 and GP8 as a function of temperature is compared in Fig. 9. According to the changing rate reflected by the slope of the curve, the thermal response of geopolymer can be divided into three phases, including phase I: water evaporation, phase II: Dihydroxylation, and phase III: Melting. In phase I, the geopolymers exhibit a rapid shrinkage, which accounts for the release of free water and dehydration of aluminosilicate gel as observed by TGA. With the increase of temperature, a deceleration period is recognized as phase II. In this phase, the gradual dihydroxylation and decomposition of aluminosilicate gel lead to a slow shrinkage as the temperature increases. Any shrinkage in Phase I and II is slow and insignificant for both GP6 and GP8 since neither any phase transitions nor melting occurs

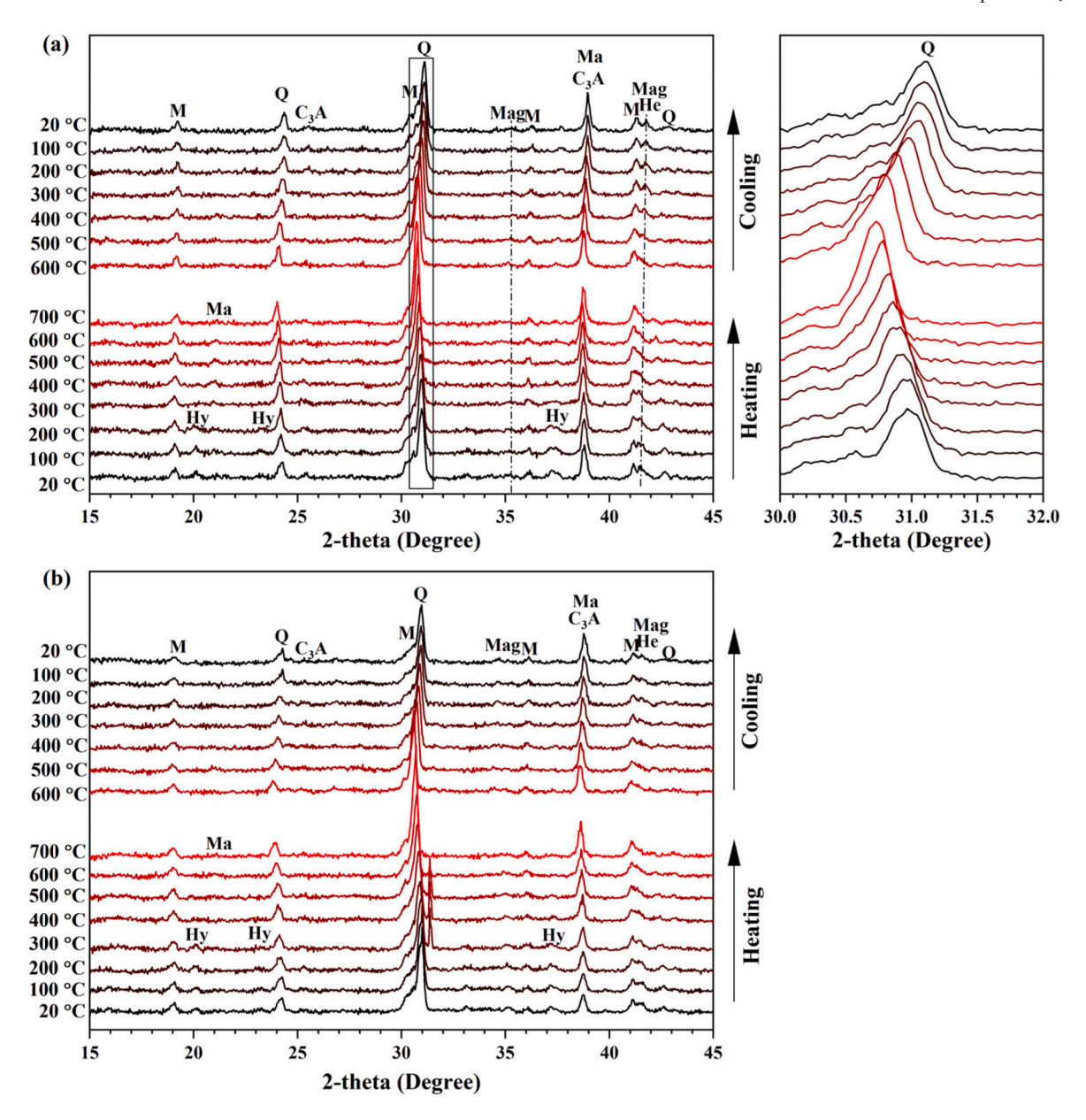


Fig. 6. The variation of crystalline patterns of specimens during heating and cooling, a) GP6 and b) GP8. (Q-Quartz, # PDF 01-085-0457, M-Mullite, # PDF 01-079-1454, C₃A- Tricalcium aluminate, # PDF 00-006-0495, Ma-Mayenite, #PDF 00-048-1882, Hy-Hydrogarnet, #PDF 01-071-0735, He-Hematite, #PDF 01-073-0603, Mag-Magnetite, #PDF 01-076-0956).

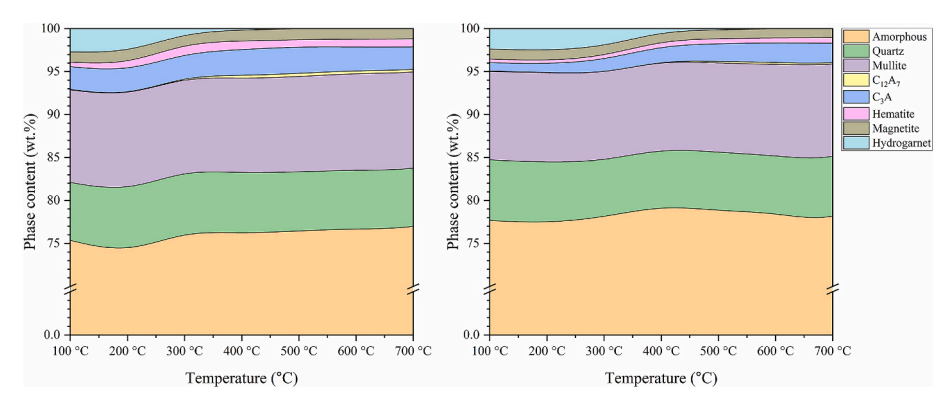


Fig. 7. In-situ high temperature XRD quantification of phase transition.

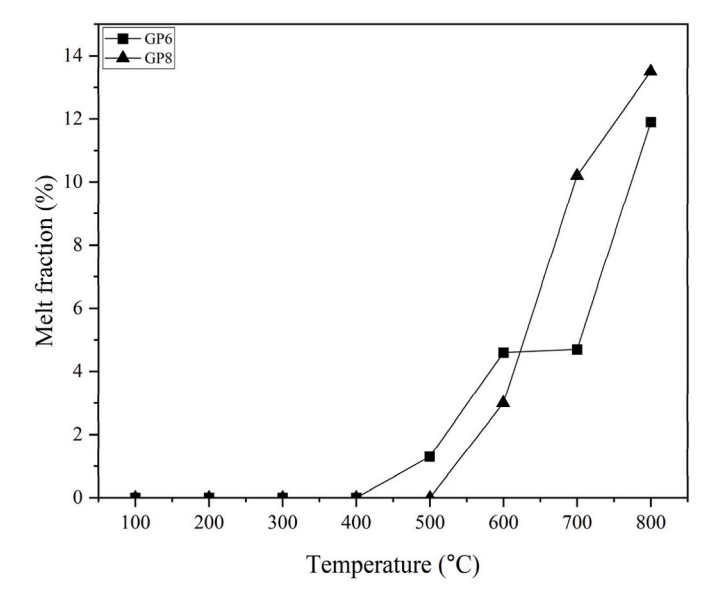
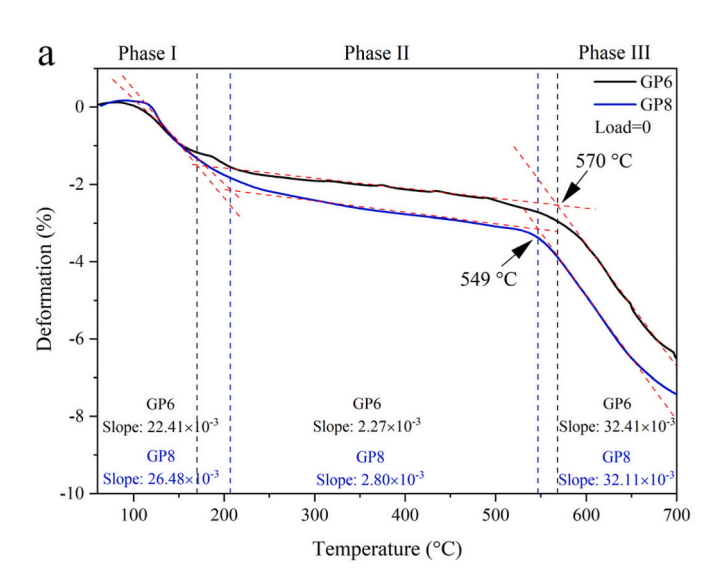


Fig. 8. The melt fraction of samples according to FactSage calculation.



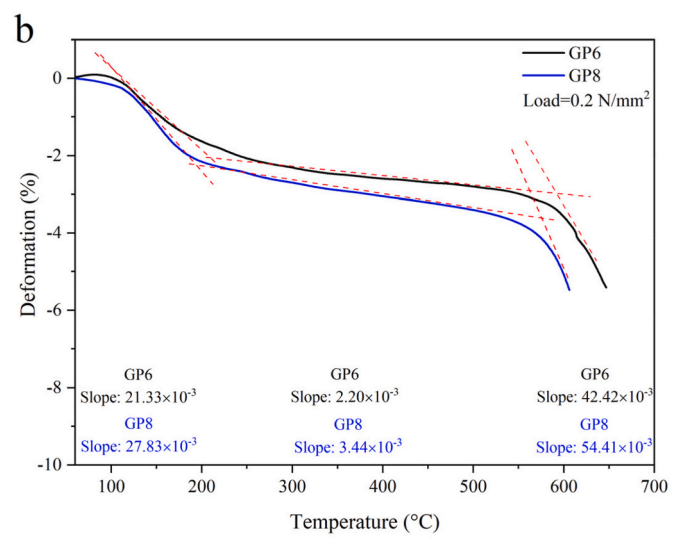


Fig. 9. The thermal linear change of geopolymers with or without loading.

according to the FactSage calculation. In terms of the effect of $Na_2O\%$, note that GP8 shows a higher shrinkage rate than GP6 in Phases I and II. Here, the dimensional change is related to two phenomena: i) Physically and chemically bonded water release, and ii) pore structure and density change. On the one hand, as deduced from the TGA results, an increased $Na_2O\%$ promotes the formation of hydration products, hence yielding a higher content of chemically bonded water to be released. On the other hand, owing to the dense matrix of GP8, a severe capillary pressure could be generated during the water release. Phase III shows the sharpest linear shrinkage after the glass transition, as observed in TGA results.

To learn the softening of material in Phase III, the deformation is further measured under a load of $0.2\ N/mm^2$ as shown in Fig. 9b. The loading has an insignificant influence on phases I and II, whereas it largely boosts the shrinkage in phase III, reaching the maximum of 5 %. It further evidences the melting in geopolymer along with the creep under load. However, according to the calculated curve slope, when it reaches the partial melting, a higher loading further increases the shrinkage rate due to the matrix softening. In comparison, the GP8 shows a more drastic shrinkage rate than the GP6 with loading. This is consistent with the FactSage thermodynamic calculation, which indicates that a high Na₂O content accelerates partial melting, leading to matrix softening above 700 °C.

3.1.4. Compressive strength test during exposure to different temperatures

The compressive strength test is performed to evaluate the mechanical evolution in situ during high temperature exposure. The testing temperatures (20, 300, 500, and 700 °C) are selected according to TGA and dilatometry analysis since the investigated samples reach specific stages at the chosen temperatures. The stress-strain curves of geopolymers at varied temperatures are depicted in Fig. 10, and the corresponding peak strain and relative compressive strength of specimens are compared in Fig. 11. Both GP6 and GP8 remain in a solid state before 500 °C, and the stress-strain curve can be divided into elastic stage, plastic stage, and post-failure stage. From 20 to 500 °C, a higher peak stress along with a larger peak strain is noticed for GP6 and GP8. In this temperature range, the stress-strain curve indicates that geopolymers shift from being brittle to becoming more ductile, especially for GP6. At the same temperature exposure, GP6 shows a lower peak stress but larger peak strain, demonstrating a lower strength but higher ductility as compared to GP8.

When comparing the stress-strain evolution between GP6 and GP8, as the temperature increases from 25 to 500 °C, an increased elastic modulus with extended ductile stage can be observed in GP6. GP8 exhibits a more linear stress-strain response with stable elastic modulus with temperature, and the corresponding peak stress and strain increase proportionally before 500 °C. This observation should be ascribed to the further reaction between precursor and activator, resulting in continuous compacting of the matrix, as verified by TGA and dilatometry results. In comparison, GP6 has lower E-modulus and less strength gain with temperature than GP8. Accordingly, two distinguished failure patterns are detected in GP6 and GP8 as depicted in Fig. 12. Among these, GP8 exhibits a spalling in the high temperature compressive test owing to its high stiffness and elasticity, while a failure-cracking pattern is detected in GP6. After 500 °C, in agreement with TGA and dilatometry results, the geopolymer paste evolves from a solid state to a viscoelastic state due to glass transition, characterized by a very low e-modulus and with strain beyond the measurement range. Herein, despite GP8 showing a higher mechanical strength before 500 °C as compared to GP6, a more thorough partial melting is noticed, exhibiting almost no strength at 700 °C. It agrees with dilatometry results that GP8 exhibits an accelerated melting coinciding with its high Na₂O%. Above all, in real fire scenario where spalling or transient failure should be avoided, GP6 with a gradual failure and large peak strain is more preferable to be used as structural material for fire resistance. On the other hand, as compared to GP8, the gradual melting of GP6 after 500 °C represents a

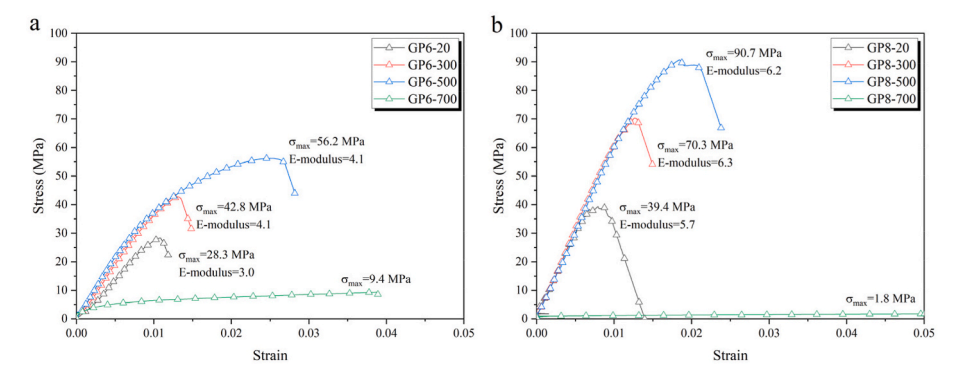


Fig. 10. Stress-strain curves of specimens at different temperatures.

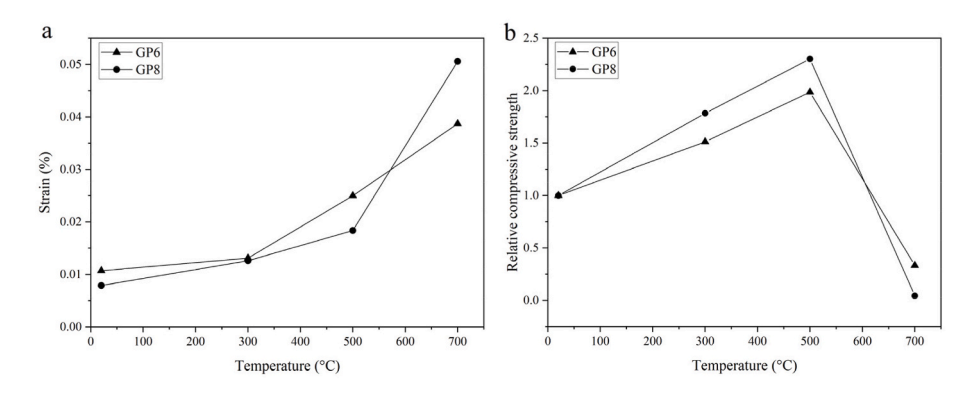


Fig. 11. (a) The strain at max yield stress and (b) relative max yield stress of specimens at different temperatures.

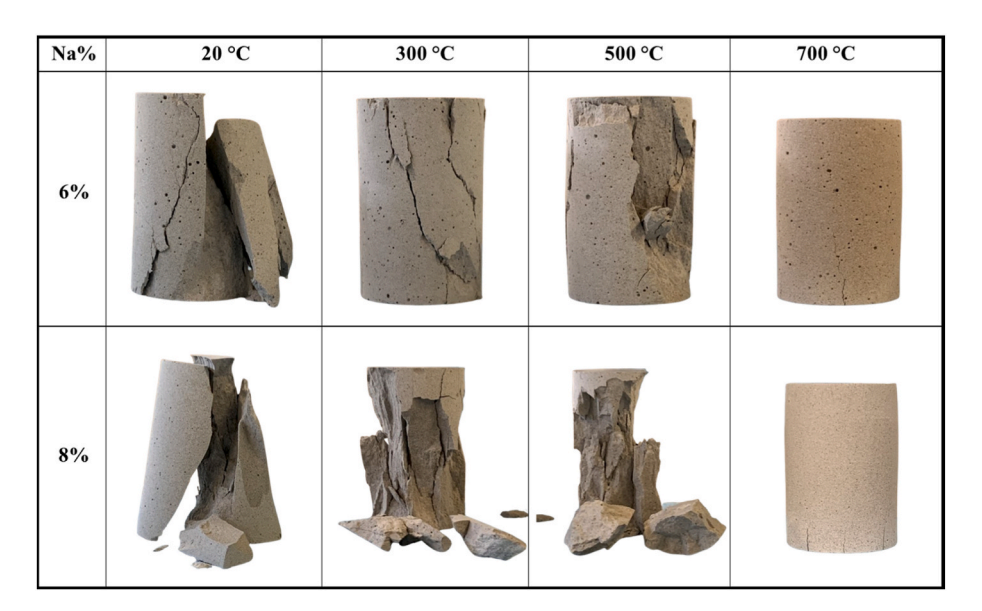


Fig. 12. Failure patterns of specimens in the in-situ compressive test.

better fire endurance performance. It offers more response time for the evacuation and rescue operations.

Interestingly, it has been reported that geopolymers with high initial strength often exhibit poor residual mechanical performance after exposure to high temperatures, attributed to a reduction in porosity [5, 15,37]. In this study, a distinctively different observation regarding in-situ high temperature behavior is found, geopolymer with high initial compressive strength show more improvement of mechanical performance with temperature as compared to geopolymer with low initial strength. The reason behind the discrepancy will be discussed in the

following section.

3.2. Ex-situ high temperature characteristics

This section pertains to samples that were heated in a muffle furnace following the identical heating procedure in in-situ high temperature characterization, and naturally cooled to room temperature. To identify the performance differences during and after thermal exposure, the post-high temperature properties of geopolymers are further investigated, including bulk characteristics, microstructure evolution, volumetric

properties, and residual mechanical strength.

3.2.1. Bulk characteristics and microstructure evolution

The morphology and EDS analysis of GP6 and GP8 are compared in Fig. 13. The bulk appearance and the 3D pore distribution of GP6 and GP8 are shown in Fig. 13a–d. Notably, GP6 shows a looser texture with numerous large pores, whereas GP8 exhibits a more compact structure with evenly distributed smaller pores, attributed to its higher reaction degree. In Fig. 13e, plenty of unreacted FA particles are noticed in GP6, and according to EDS analysis, a low calcium N-A-S-H gel is observed as the dominant binder. In comparison, a co-existence of N-A-S-H gel and dense C-A-S-H gel wrapping around unreacted LS particles is noticed in GP8. More detailed information about gel characters can be found in our previous study [23], and the co-existence of N-A-S-H and C-A-S-H gel has been reported due to the unique reaction process of LS, especially for a system with high alkaline content.

The microstructure post-exposure of geopolymers as a function of temperature is visualized in Fig. 14 using SEM and μ-CT. Accordingly, the pore size distribution of specimens is calculated using Micro-CT, as shown in Fig. 15. It should be noted that the calculated porosity only accounts for pores larger than $11.4 \mu m$, due to the resolution limit of the micro-CT. From room temperature to 700 °C, both GP6 and GP8 exhibit a denser microstructure with reduced porosity and a shift toward smaller pore sizes. This observation is, on the one hand, related to the thermally induced shrinkage. On the other hand, as aforementioned, the melted phase fills the small pores and densifies the matrix owing to partial melting. This phenomenon is particularly evident in GP8, especially at 700 °C, due to its compact structure with a predominance of small pores compared to GP6. While at the macro level, as noticed by μ-CT, drastic macro cracking occurred in GP8 after being exposed to 700 °C, which is related to thermal incompatibilities during cooling. The matrix of GP8 is stiff after 700° exposure, that the thermal stress built up

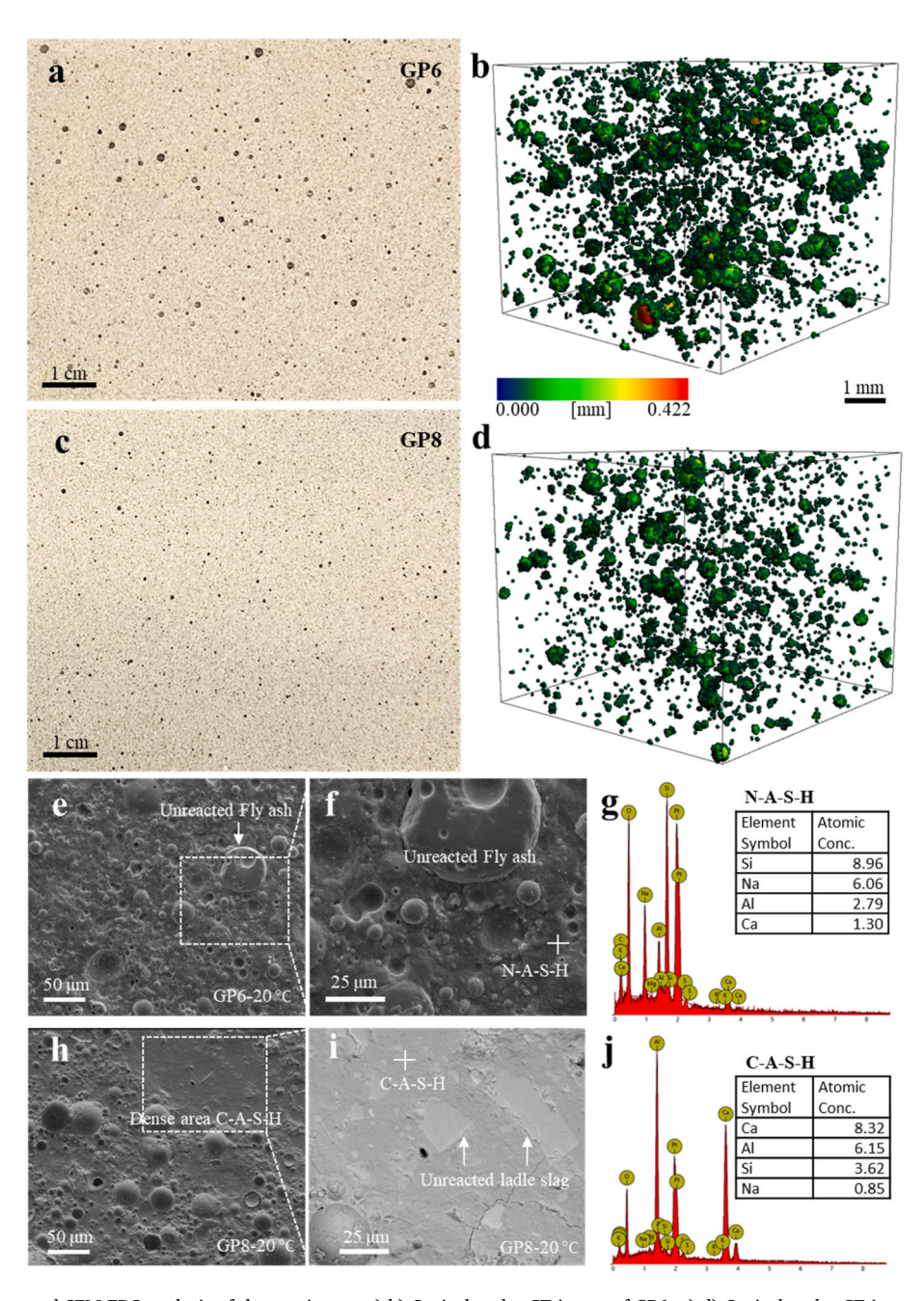


Fig. 13. The bulk structure and SEM-EDS analysis of the specimens, a)-b) Optical and u-CT image of GP6. c)-d) Optical and u-CT image of GP8, e)-f) SEM-EDX of GP6, and h)-i) SEM-EDX of GP8.

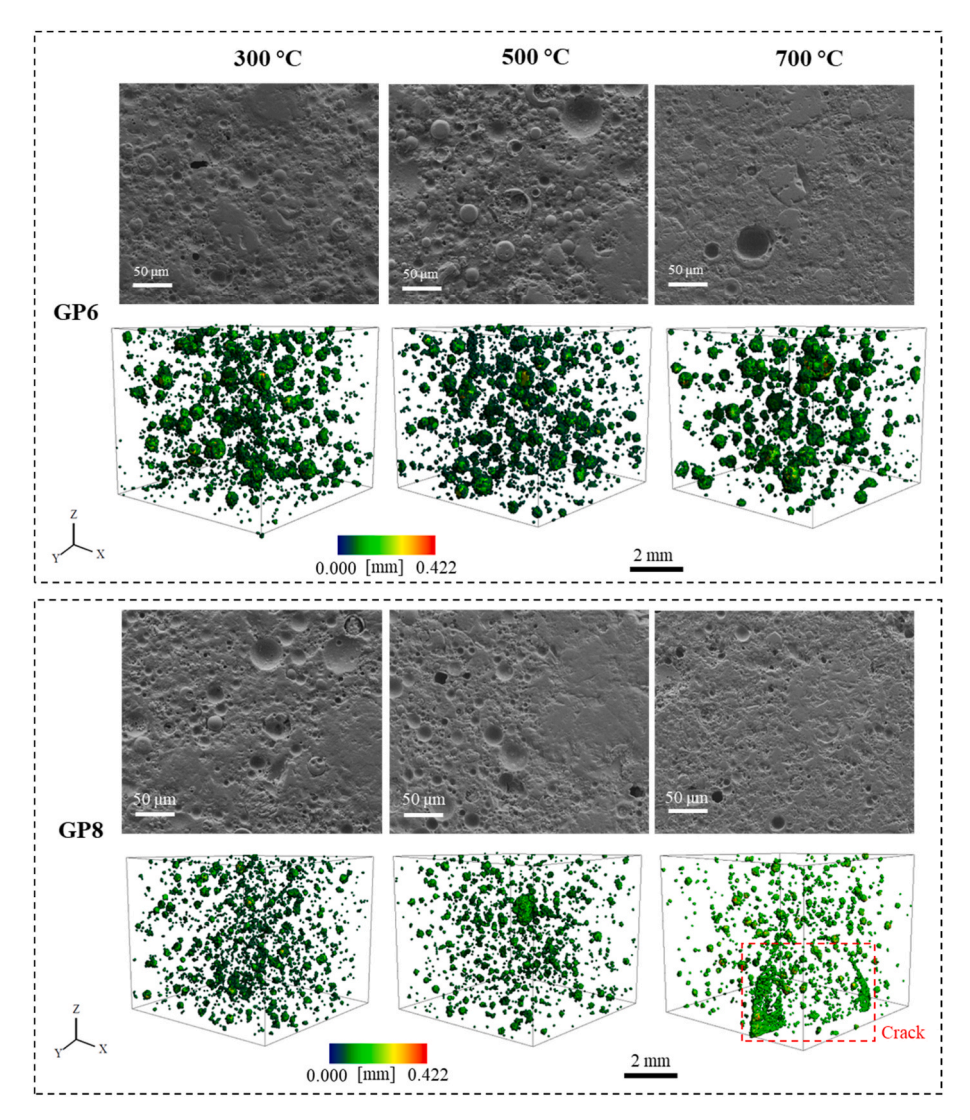


Fig. 14. The microstructure evolution of specimens at different temperatures.

during cooling leads to cracking. In Fig. 16, the variation of bulk density at different temperatures correlates well with microstructure observation. In comparison, a higher bulk density is detected in GP8 owing to the promoted reaction degree. As the temperature increases, both GP6 and GP8 exhibit a relatively constant bulk density up to $500\,^{\circ}$ C, followed by a rapid densification at $700\,^{\circ}$ C, which is attributed to the partial melting and sintering discussed above. Among these, GP8 exhibits a higher bulk density as compared to GP6 after being exposed to high temperatures. While different from the dilatometry (Fig. 9), as shown in Fig. 16b, a similar shrinkage is detected in both GP6 and GP8 after thermal exposure. But both values are very similar, indicating that the drastic shrinkage has already taken place at the highest temperature.

3.2.2. Mechanical strength after thermal exposure

The compressive strength test is performed on geopolymers after exposure to elevated temperatures, and the results are shown in Fig. 17. And the failure pattern of samples are shown in Fig. 18. The stress-strain curves for both GP6 and GP8 show an increase in stress and a reduction in creep strain with rising temperature, indicating an increase in stiffness. With the temperature increasing from 20 to 700 °C, the residual strength of GP6 increases from 29.5 to 53.2 MPa. Similarly, for GP8, a continuous residual strength gain from 36.1 to 54.0 MPa is recorded up to 500 °C. After being exposed to 700 °C, GP8 experiences a drastic cracking, which makes it unusable for the compressive strength test. The

visual appearance of samples after high temperature exposure is provided in Appendix Fig. A1. In Fig. 18, GP6 exhibits a failure-cracking pattern up to 700 °C. GP8 shows a spalling pattern at ambient temperature but a failure-cracking pattern at high temperatures. The observation is different from in-situ compressive test, especially at 700 °C. This is because the matrix transits from an elastic state to a solid state during cooling, with the formation of inner cracks, which changes the failure pattern and negatively impacts the strength enhancement. This phenomenon is more drastic in GP8. On the one hand, the GP8 experiences severer shrinkage after high temperature exposure as compared to GP6. On the other hand, the high stiffness matrix due to drastic matrix impaction and densification has a limited capacity to withstand the internal stress and deformation during cooling [37]. In this case, a lower strength gain ratio is obtained in GP8 after high temperature exposure.

4. Discussion

4.1. The in-situ thermal behavior of geopolymers

When exposed to elevated temperatures, three critical stages of transition in geopolymers are detected in this work, namely water evaporation, gel dehydration-dihydroxylation, and melting. The first stage is dominated by the loss of physically and chemically bonded water. According to TGA and dilatometry analysis, the evaporation of

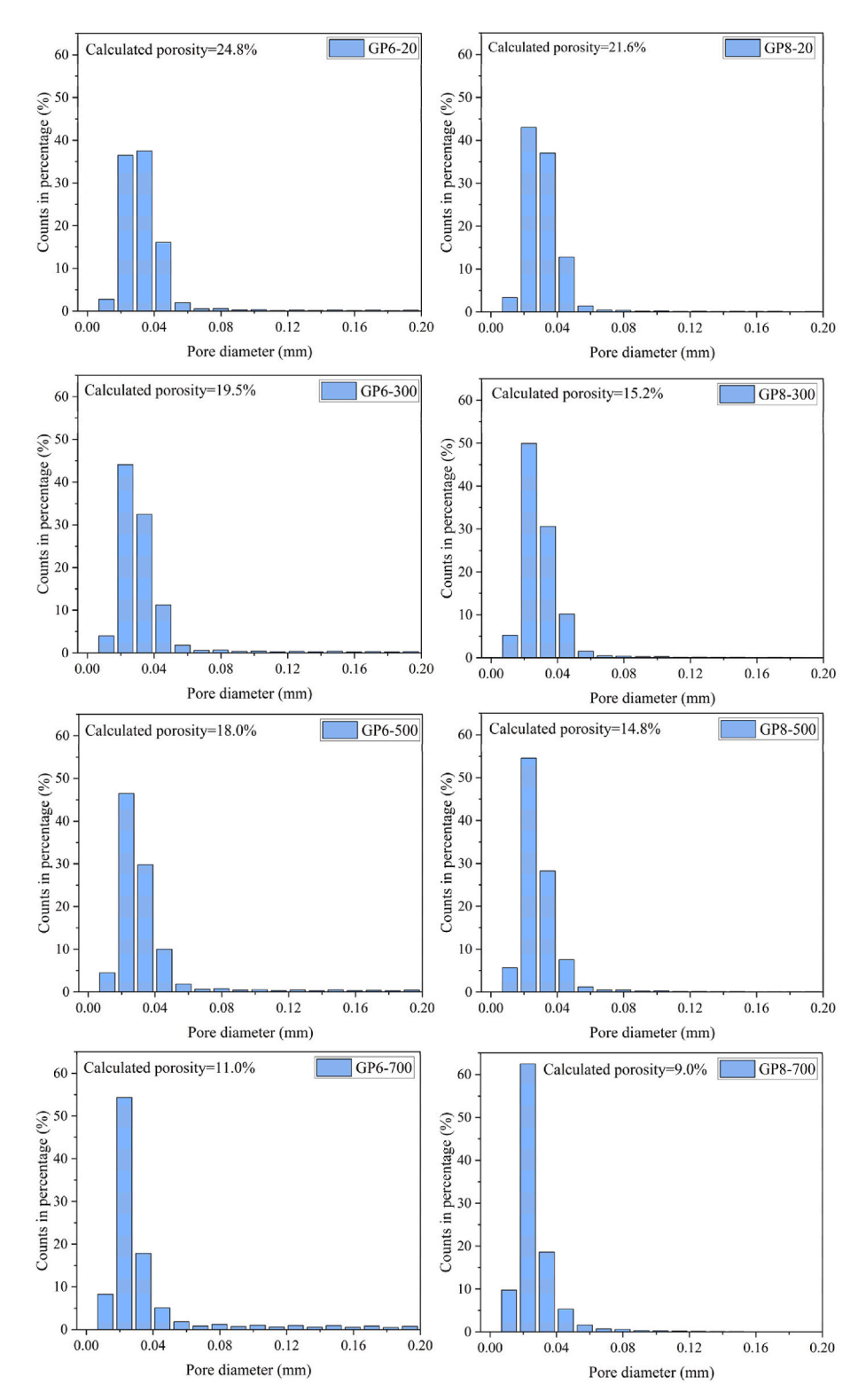


Fig. 15. Pore size distribution at different temperatures from Micro-CT.

free and condensed water leads to a significant shrinkage before 200 $^{\circ}\text{C}.$ In this stage, owing to the promoted reaction degree and densified microstructure, more water release is detected in GP8 as compared to GP6, accompanied by a higher shrinking rate. In the second stage, further geopolymerization, as well as gradual dihydroxylation and partial decomposition of aluminosilicate gel, occurred sequentially, resulting in a slow shrinkage in a prolonged period from 200 to 550 $^{\circ}\text{C}.$ Accordingly, the high Na₂O% geopolymer experiences a higher

shrinkage rate than that of geopolymer with a lower $\rm Na_2O\%$. On the one hand, this should result from the enhanced further geopolymerization in GP6, due to its relatively low reaction degree with plenty of unreacted precursors at the onset of Phase II. On the other hand, GP8 with higher reaction degree (gel content) is prone to undergo a more pronounced gel dihydroxylation during this stage. The third stage starts from approximately 550 °C as geopolymers reach the glass transition temperature, in which the sharpest shrinkage is detected within the investigated

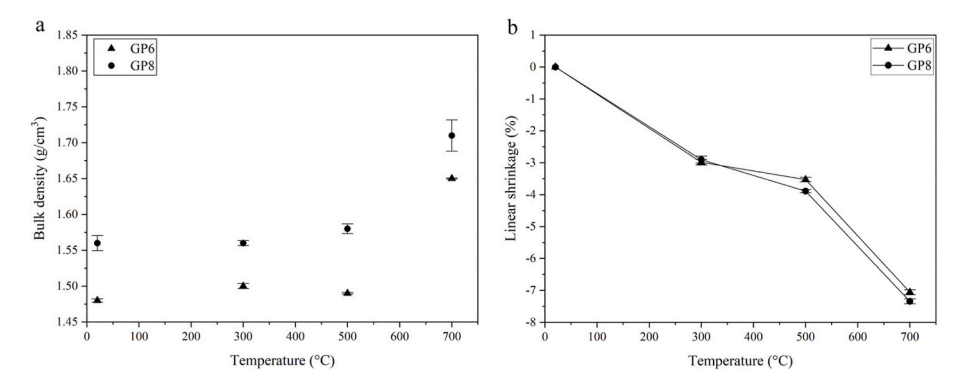


Fig. 16. The bulk density and deformation of specimens after exposure at high temperatures.

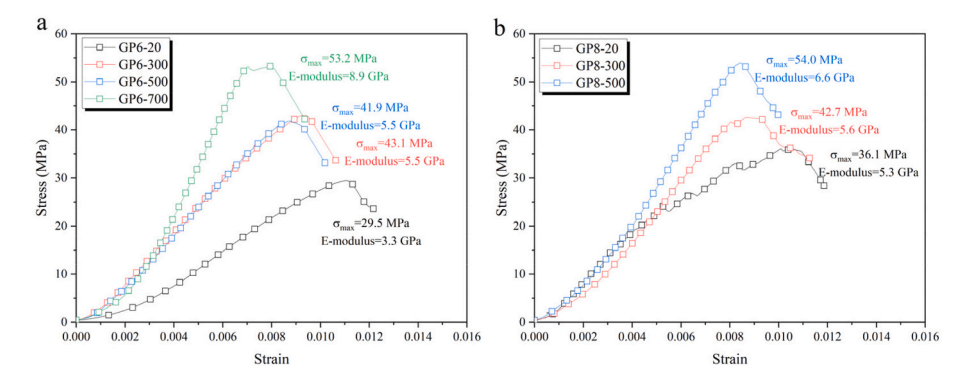


Fig. 17. Compressive strength of specimens after high-temperature exposure.

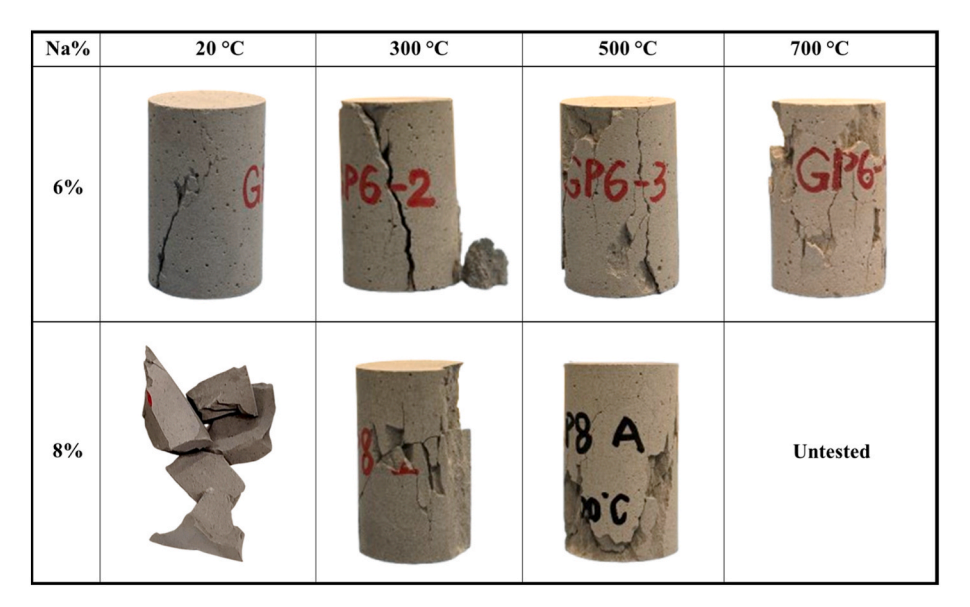


Fig. 18. Failure pattern of samples in the compressive strength test.

temperature range. Notably, the GP6 and GP8 exhibit a similar onset temperature of the third stage. It indicates that the reaction degree of geopolymer plays an insignificant role in determining the starting of glass transition, which infers that the glass transition of geopolymers should be dominated by intrinsic properties, such as precursor composition. However, according to dilatometry and in-situ compressive test results (Figs. 9 and 10), a higher reaction degree/Na $_2$ O% largely promotes the melting rate of geopolymer.

The in-situ high-temperature mechanical performance is largely correlated to the aforementioned physicochemical transition as a

function of temperature. Within the investigated temperature, the insitu compressive strength of geopolymers increases with temperature, until it reaches the partial melting. Here, it is well-established that the geopolymer strength increase below 300 °C should be related to continuous chemical condensation, namely further geopolymerization [12,14]. In addition, Pan and Sanjayan [17] concluded that the strength increase in the range of 380–520 °C is either due to the stiffening of the geopolymer gel or the promoted surface force among gel particles induced by moisture removal. The observation from this work is in good agreement with this study. With continuous water release induced by

temperature, the stiffness, as well as elastic modulus of geopolymers increases. While it is worth noting that simultaneously, an increase in creep strain is detected along with temperature, demonstrating an enhancement in the ductility of geopolymers. As compared to GP6, GP8 with a denser matrix experiences more thermal compacting, contributing to higher in-situ compressive strength with rapid strength gain before partial melting.

Interestingly, previous studies examining the post-high-temperature behavior of geopolymers have concluded that the stiffness of the matrix adversely affects thermal performance, particularly mechanical strength, as high stiffness limits the matrix's ability to accommodate thermal stress. However, it is observed in this study that during high temperature exposure, the highly reacted geopolymer with high stiffness shows superior mechanical performance over the under-reacted geopolymer. This discrepancy should be due to the fact that when exposed to high temperature, the matrix gradually shifts from a solid to a viscoelastic state due to glass transition. In this process, it is highly possible that geopolymers with enhanced ductility could accommodate the thermal stress and incompatibilities, in avoiding cracking. Simultaneously, the matrix with high stiffness undergoes severe thermal compaction, resulting in better mechanical performance before partial melting.

4.2. The discrepancy between in-situ and ex-situ performance of geopolymer

The major finding of this study is that there is a significant difference between in-situ and ex-situ performance of geopolymers, concerning thermal shrinkage, compressive strength, and creep strain. To clarify the discrepancy among these processes, the thermal deformation of geopolymers during and after exposure to elevated temperatures is compared in Fig. 19a. It is observed that both GP6 and GP8 experienced additional shrinkage during the cooling phase. This phenomenon is well established in ceramic and geological materials, which mainly resulted from the further matrix compaction during cooling. Notably, GP6 exhibits a larger shrinkage during cooling at all examined temperatures. This can be attributed to its porous structure, which is susceptible to

shrinkage during the cooling process. In comparison, GP8 shows a minimal difference between the in-situ and ex-situ thermal deformation, especially at 700 $^{\circ}$ C. It implies that the dense matrix of GP8 is reluctant to further compaction during cooling.

As seen in Fig. 19b, after cooling, a significant reduction in strength is observed in geopolymers compared to their in-situ compressive strength at high temperature, with the disparity increasing at higher temperatures. Among these, GP8 with a higher reaction degree exhibits a significant strength loss while that of GP6 is less prominent, even though a larger shrinkage difference is noticed in GP6 between in-situ and ex-situ conditions. As for the strain at yield stress in Fig. 19c, the corresponding strain during high temperature exposure is larger than that of geopolymer after high temperature exposure. On the other hand, during thermal exposure, the strain at yield stress increases with temperature while an opposite trend is observed in ex-situ. This further confirms that high temperatures increase the ductility of geopolymer.

However, as it cools to ambient temperature, the matrix transfers from a viscoelastic to a solid form. In this case, geopolymer with decreased ductility and increased brittleness manifests increased susceptibility to thermal deformation, which therefore, is prone to structural degradation and cracking [37]. This is supported by the Micro-CT results in Fig. 14. Consequently, a strength deterioration during cooling is resulted. In this case, matrix cracking during the cooling process plays a dominant role, negatively affecting the strength evolution of geopolymers. In a dense matrix like GP8, the high stiffness accompanying severe shrinkage induces drastic cracking during cooling, which results in a significant strength difference between the in-situ strength and residual strength. In contrast, GP6 with low stiffness and high porosity can accommodate the inner stress during cooling, which largely preserves the structural stability. Therefore, GP6 exhibits an insignificant cooling induced strength reduction before 500 °C. After 700 °C, even a higher residual strength is recovered for GP6 due to the matrix solidification. Accordingly, even for a highly porous matrix, it can be inferred that in active cooling conditions, a higher cooling rate could further increase inner stresses, negatively impacting structural stability and residual performance.

In addition, it should be mentioned that, as observed in the in-situ

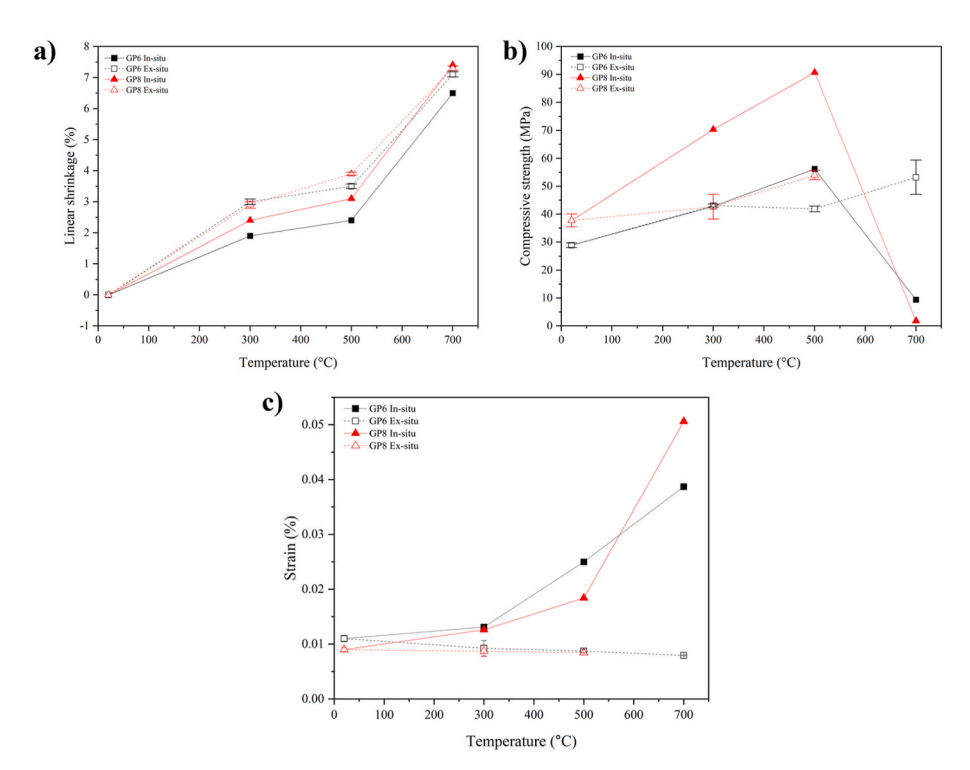


Fig. 19. The behavior of geopolymers during and after high temperature exposure, a) thermal shrinkage, b) compressive strength, and c) strain at yield stress.

XRD test, the crystalline phases, such as quartz undergo thermal expansion/contraction during the heating and cooling process. This crystal deformation may pose varied influence during heating, depending on the amount of crystal and the ductility of the matrix. In contrast, it may exert a certain negative impact on the matrix during cooling, since the increased brittleness further hinders its capacity to accommodate crystal deformation, especially for highly reacted geopolymer.

In conclusion, a different thermal evolution is observed in geopolymers during heating and cooling. When exposed to elevated temperature, the geopolymer with high stiffness enables superior in-situ mechanical performance, owing to the simultaneous ductility enhancement. Nevertheless, geopolymer is negatively influenced by matrix stiffness during cooling due to the reduced ability to accommodate thermal incompatibility, resulting in cracking and strength loss, especially for geopolymers with high stiffness. Therefore, findings from ex-situ studies of geopolymers introduce bias when predicting their insitu high temperature performance.

4.3. Limitations and outlooks

This work aims to capture the intrinsic material behavior of geopolymer under thermal exposure using in-situ techniques, and compare with previous findings based on ex-situ characterizations using similar testing settings. Thus, a repeatable and comparable methodology was applied to characterize how geopolymers evolve under high temperatures from fundamental perspectives, without considering additional environmental variables. It should be noted that, in addition to the intrinsic properties of the material, the thermal behavior of geopolymer is also affected by the environmental conditions, such as structural loading, fire level, and complex cooling scenarios. In this case, the findings from this study still have inherent constraints in directly predicting geopolymer behavior in real fire cases. These results should be used as a reference for future efforts to improve the understanding and prediction of geopolymer performance in more realistic fire conditions. Based on the present findings, the following outlooks for future research are suggested:

Firstly, to understand the mechanical performance of geopolymers at the hot state, the load was applied when the geopolymer reached thermal equilibrium at elevated temperatures. However, in a real fire scenario, the infrastructure is under load during thermal exposure. The loading may additionally impact the thermal behavior of geopolymers, especially the deformation and melting, as observed in Fig. 9. Thus, future research on the thermal performance of geopolymers under load is essential to deepen the understanding of mechanical behavior in structural applications.

Secondly, in this work, a fixed heating rate was applied in in-situ tests according to the standard (EN 993-8), and specimens were naturally cooled to ambient temperature. However, in case of fire, on the one hand, the heating rate could be varied by the level of fire. On the other hand, this study applied natural cooling in order to make a comparison to previous geopolymer research [5,9,12,25]. In real fire hazards, the cooling of infrastructure is influenced by the fire extinguishing methodology, including active and passive fire protection. For example, with a water extinguishing, the high cooling rate may lead to drastic thermal shock, which may result in spalling, rapid cracking, and drastic structural failure. On top of the current findings, higher heating or cooling rate could adversely affect geopolymer performance due to thermal disequilibrium [9,22,38]. In this case, the effect of heating and cooling rates on the in-situ behavior of geopolymers should be verified in future studies.

Thirdly, this study examined the in-situ thermal behavior of geopolymers up to 700 $^{\circ}$ C, until the partial melting was reached. Nevertheless, this temperature remains lower than those typically encountered in real fire scenarios. To fully capture the thermal evolution of the material, thermal exposure to more extreme temperatures is

warranted.

5. Conclusions

This study provides a comprehensive understanding of the response of geopolymers at elevated temperatures from the perspectives of phase dehydration, crystalline transition, deformation, and mechanical properties. In addition, the in-situ behavior is compared with the residual properties of thermally exposed geopolymers, including microstructure, deformation, and residual mechanical properties. The experimental results lead to the following conclusions:

During heating, the crystalline phase assemblage in geopolymers remains largely stable, with hydrogarnet decomposing up to 400 $^{\circ}$ C. Some phases (e.g., quartz, iron oxide) undergo phase transitions. High Na₂O% lowers the melting point of silicates and largely accelerates the softening of geopolymers at high temperatures. In this case, well-reacted geopolymer with high Na₂O% experiences a higher shrinkage rate than under-reacted geopolymer during heating, owing to both severe gel dihydroxylation and accelerated partial melting.

As the matrix transitions from a solid to a viscoelastic state, the increasing ductility of geopolymers with temperature plays a pivotal role in accommodating thermal incompatibilities and maintaining structural integrity. Below 500 °C, both in-situ compressive strength and strain at peak stress increase with temperature. Geopolymer with dense matrix and high stiffness exhibits a more linear stress-strain response and prominent strength gain before 500 °C. However, strength drops sharply around 550 °C due to partial melting, regardless of reaction degree or matrix compactness.

A significant discrepancy is observed between in-situ and ex-situ thermal performance of geopolymers. Geopolymer matrix transforms from viscoelastic to a solid state during the cooling process, accompanied by a reduction in ductility and further shrinkage. It leads to matrix deterioration, cracking, and negatively impacts the residual performance of geopolymers, especially in a dense matrix with high stiffness and low ductility. Thus, matrix stiffness and compactness benefit in-situ but hinder residual mechanical performance. Ex-situ studies can lead to biased predictions on in-situ high-temperature performance.

Before partial melting, geopolymers exhibit excellent in-situ mechanical performance. Notably, the increase of failure stress and creep strain with temperature holds a significant advantage for evacuation and rescue operations. Nevertheless, when it reaches the melting temperature, the drastic shrinkage and matrix softening are the major challenges for high temperature applications. Future research must consider both partial melting and cooling induced matrix changes to reliably assess high temperature performance.

CRediT authorship contribution statement

Y. Luo: Writing – original draft, Methodology, Investigation, Funding acquisition, Formal analysis, Data curation. K.M. Klima: Investigation. S. Melzer: Investigation. H.J.H. Brouwers: Writing – review & editing, Supervision, Funding acquisition. Qingliang Yu: Writing – review & editing, Supervision, Project administration, Methodology, Investigation, Funding acquisition, Conceptualization.

Declaration of competing interest

The authors declare that they have no known competing financial interests or personal relationships that could have appeared to influence the work reported in this paper.

Acknowledgments

This research is carried out under China Scholarship Council (No. 201906370011) and the Department of the Built Environment at Eindhoven University of Technology. The authors gratefully acknowledge

Prof. Dr. S.R. van der Laan (Eindhoven University of Technology and Tata Steel, The Netherlands) for the discussion on the thermal behaviours of geopolymers and for editing the paper. Special thanks are given

to P. Put (Tata Steel, The Netherlands) and P. van den Idsert (Tata Steel, The Netherlands) for their help with in-situ high temperature tests.

Appendix

Table A1

The phase composition of samples at different temperatures determined by in-situ high temperature XRD-Rietveld analysis.

GP6								
Temperature	Quartz	Mullite	Mayenite	C3A	Hematite	Magnetite	Hydrogarnet	Amorphous
100	6.737 (0.116)	10.788 (0.33)	0.044 (0.062)	2.659 (0.132)	0.519 (0.121)	1.182 (0.098)	2.717 (0.214)	75.3549 (0.4618)
200	7.179 (0.119)	11.12 (0.344)	0.034 (0.061)	2.844 (0.136)	0.835 (0.142)	1.384 (0.099)	2.797 (0.213)	73.806 (0.4795)
300	7.141 (0.114)	10.812 (0.337)	0.081 (0.057)	2.676 (0.129)	1.166 (0.138)	1.18 (0.095)	0.486 (0.155)	76.46 (0.4459)
400	7.006 (0.123)	11.013 (0.365)	0.37 (0.061)	3.044 (0.139)	1.001 (0.147)	1.278 (0.102)	0.143 (0.103)	76.1454 (0.4626)
500	6.883 (0.131)	11.065 (0.396)	0.377 (0.065)	3.116 (0.148)	0.816 (0.156)	1.282 (0.109)	0.001 (0.112)	76.4602 (0.499)
600	6.816 (0.138)	11.278 (0.434)	0.329 (0.072)	2.711 (0.159)	0.928 (0.173)	1.22 (0.118)	0	76.7179 (0.5437)
700	6.816 (0.138)	11.278 (0.434)	0.329 (0.072)	2.711 (0.159)	0.928 (0.173)	1.22 (0.118)	0	76.7179 (0.5437)
GP8								
Temperature	Quartz	Mullite	Mayenite	C3A	Hematite	Magnetite	Hydrogarnet	Amorphous
100	7.071 (0.126)	10.282 (0.343)	0.047 (0.065)	0.974 (0.129)	0.425 (0.117)	1.168 (0.104)	2.372 (0.229)	77.6621 (0.4813)
200	7.032 (0.126)	10.476 (0.353)	0.02 (0.065)	0.991 (0.13)	0.363 (0.106)	1.194 (0.105)	2.564 (0.231)	77.36 (0.4869)
300	6.533 (0.139)	10.179 (0.397)	0.011 (0.071)	1.551 (0.155)	0.45 (0.163)	1.132 (0.113)	2.105 (0.251)	78.0399 (0.5553)
400	6.631 (0.138)	10.241 (0.406)	0	1.733 (0.154)	0.599 (0.164)	1.066 (0.114)	0.3 (0.202)	79.431 (0.5412)
500	6.808 (0.137)	10.355 (0.406)	0.207 (0.067)	2.077 (0.152)	0.597 (0.161)	1.011 (0.112)	0.134 (0.118)	78.8103 (0.5128)
600	6.639 (0.132)	10.611 (0.396)	0.256 (0.065)	2.262 (0.148)	0.573 (0.157)	1.078 (0.109)	0.001 (0.111)	78.5804 (0.4987)
700	7.199 (0.146)	11.112 (0.45)	0.139 (0.074)	2.451 (0.159)	0.641 (0.109)	1.072 (0.117)	0	77.3861 (0.5295)

Table A2
The input data for FactSage calculation, excluding inert quartz, mulite, and magnetite

GP6		GP8	
Na ₂ O	14.704	Na ₂ O	17.182
MgO	1.08	MgO	1.03
Al_2O_3	10.567	Al_2O_3	9.643
SiO_2	35.752	SiO_2	35.086
P_2O_5	0.216	P_2O_5	0.196
SO_3	0.435	SO_3	0.436
K ₂ O	1.09	K ₂ O	1.023
CaO	7.442	CaO	6.955
TiO_2	0.541	TiO_2	0.511
V_2O_5	0.014	V_2O_5	0.012
Cr ₂ O ₃	0.014	Cr_2O_3	0.016
MnO	0.074	MnO	0.068
Fe ₂ O ₃	3.444	Fe_2O_3	3.284
Fe ₂ O ₃		Fe_2O_3	
corresponds to		corresponds to	
81.3 wt.% of ma	terial	81.6 wt.% of ma	iterial

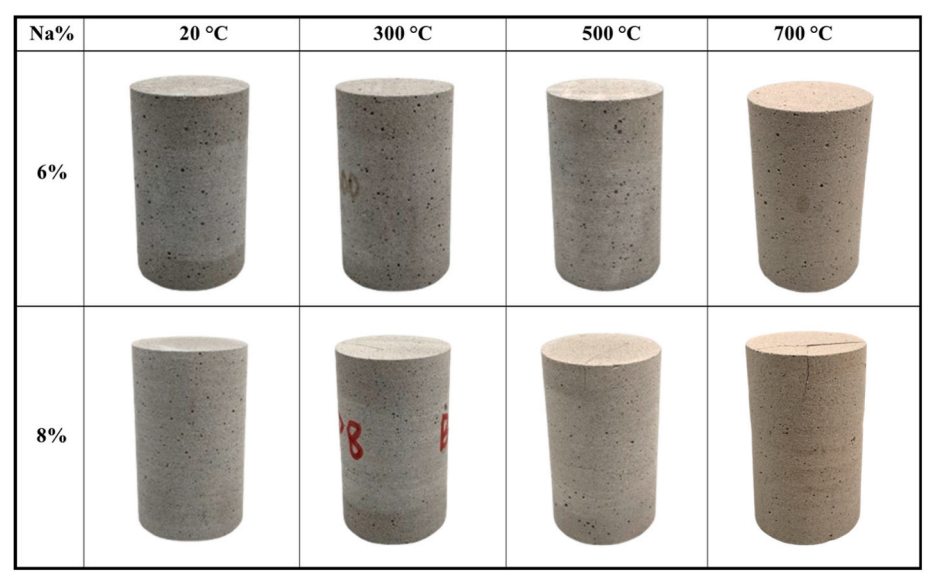


Fig. A1. The visual appearance of samples after exposure to high temperatures.

Data availability

Data will be made available on request.

References

- [1] P. Duxson, A. Fernández-Jiménez, J.L. Provis, G.C. Lukey, A. Palomo, J.S.J. van Deventer, Geopolymer technology: the current state of the art, J. Mater. Sci. 42 (2007) 2917–2933, https://doi.org/10.1007/s10853-006-0637-z.
- [2] C. Shi, A.F. Jiménez, A. Palomo, New cements for the 21st century: the pursuit of an alternative to Portland cement, Cement Concr. Res. 41 (2011) 750–763, https:// doi.org/10.1016/j.cemconres.2011.03.016.
- [3] J.L. Provis, S.A. Bernal, Geopolymers and related alkali-activated materials, Annu. Rev. Mater. Res. 44 (2014) 299–327, https://doi.org/10.1146/annurev-matsci-070813-113515.
- [4] J.L. Provis, Geopolymers and other alkali activated materials: why, how, and what? Mater. Struct. 47 (2014) 11–25, https://doi.org/10.1617/s11527-013-0211-5.
- [5] M. Lahoti, K.H. Tan, E.-H. Yang, A critical review of geopolymer properties for structural fire-resistance applications, Constr. Build. Mater. 221 (2019) 514–526, https://doi.org/10.1016/j.conbuildmat.2019.06.076.
- [6] P. Duxson, G.C. Lukey, J.S.J. van Deventer, Thermal evolution of metakaolin geopolymers: Part 1 – physical evolution, J. Non-Cryst. Solids 352 (2006) 5541–5555, https://doi.org/10.1016/j.jnoncrysol.2006.09.019.
- [7] P. Duxson, G.C. Lukey, J.S.J. van Deventer, The thermal evolution of metakaolin geopolymers: Part 2 – phase stability and structural development, J. Non-Cryst. Solids 353 (2007) 2186–2200, https://doi.org/10.1016/j.jnoncrysol.2007.02.050.
- [8] Y. Luo, High-temperature Resistant Geopolymer-Based Materials Out of Industrial Residuals: from Understanding to Development and Optimization, Eindhoven University of Technology, 2024. Phd Thesis (Research TU/e/Graduation TU/e).
- [9] W. Tu, M. Zhang, Behaviour of alkali-activated concrete at elevated temperatures: a critical review, Cement Concr. Compos. 138 (2023) 104961, https://doi.org/ 10.1016/j.cemconcomp.2023.104961.
- [10] M. Lahoti, K.K. Wong, E.-H. Yang, K.H. Tan, Effects of Si/Al molar ratio on strength endurance and volume stability of metakaolin geopolymers subject to elevated temperature, Ceram. Int. 44 (2018) 5726–5734, https://doi.org/10.1016/j. ceramint.2017.12.226.
- [11] M. Lahoti, K.K. Wong, K.H. Tan, E.-H. Yang, Effect of alkali cation type on strength endurance of fly ash geopolymers subject to high temperature exposure, Mater. Des. 154 (2018) 8–19, https://doi.org/10.1016/j.matdes.2018.05.023.
- [12] K.M. Klima, K. Schollbach, H.J.H. Brouwers, Q. Yu, Thermal and fire resistance of Class F fly ash based geopolymers – a review, Constr. Build. Mater. 323 (2022) 126529, https://doi.org/10.1016/j.conbuildmat.2022.126529.
- [13] M. Lahoti, S.F. Wijaya, K.H. Tan, E.-H. Yang, Tailoring sodium-based fly ash geopolymers with variegated thermal performance, Cement Concr. Compos. 107 (2020) 103507, https://doi.org/10.1016/j.cemconcomp.2019.103507.
- [14] Y. Luo, S.H. Li, K.M. Klima, H.J.H. Brouwers, Q. Yu, Degradation mechanism of hybrid fly ash/slag based geopolymers exposed to elevated temperatures, Cement Concr. Res. 151 (2022) 106649, https://doi.org/10.1016/j. cemconres.2021.106649.

- [15] W.D.A. Rickard, C.S. Kealley, A. van Riessen, Thermally induced microstructural changes in fly ash geopolymers: experimental results and proposed model, J. Am. Ceram. Soc. 98 (2015) 929–939, https://doi.org/10.1111/jace.13370.
- [16] D.L.Y. Kong, J.G. Sanjayan, Effect of elevated temperatures on geopolymer paste, mortar and concrete, Cement Concr. Res. 40 (2010) 334–339, https://doi.org/ 10.1016/j.cemconres.2009.10.017.
- [17] Z. Pan, J.G. Sanjayan, Stress-strain behaviour and abrupt loss of stiffness of geopolymer at elevated temperatures, Cement Concr. Compos. 32 (2010) 657–664, https://doi.org/10.1016/j.cemconcomp.2010.07.010.
- [18] D.E. Day, Mixed alkali glasses their properties and uses, J. Non-Cryst. Solids 21 (1976) 343–372, https://doi.org/10.1016/0022-3093(76)90026-0.
- [19] A. Fernández-Jiménez, A. Palomo, J.Y. Pastor, A. Martín, New cementitious materials based on alkali-activated fly ash: performance at high temperatures, J. Am. Ceram. Soc. 91 (2008) 3308–3314, https://doi.org/10.1111/j.1551-2916.2008.02625.x.
- [20] Z. Pan, J.G. Sanjayan, Factors influencing softening temperature and hot-strength of geopolymers, Cement Concr. Compos. 34 (2012) 261–264, https://doi.org/ 10.1016/j.cemconcomp.2011.09.019.
- [21] C. Wang, Y. Fang, X. Wang, H. Yang, F. Xing, Compressive properties of sustainable geopolymers at elevated temperatures: strength and elastic modulus evolution, Constr. Build. Mater. 411 (2024) 134515, https://doi.org/10.1016/j. conbuildmat.2023.134515.
- [22] H. Wu, X. Lin, A. Zhou, A review of mechanical properties of fibre reinforced concrete at elevated temperatures, Cement Concr. Res. 135 (2020) 106117, https://doi.org/10.1016/j.cemconres.2020.106117.
- [23] Y. Luo, H.J.H. Brouwers, Q. Yu, Understanding the gel compatibility and thermal behavior of alkali activated Class F fly ash/ladle slag: the underlying role of Ca availability, Cement Concr. Res. 170 (2023) 107198, https://doi.org/10.1016/j. cemeonres.2023.107198.
- [24] Y. Luo, K.M. Klima, H.J.H. Brouwers, Q. Yu, Effects of ladle slag on Class F fly ash geopolymer: reaction mechanism and high temperature behavior, Cement Concr. Compos. 129 (2022) 104468, https://doi.org/10.1016/j. cemconcomp. 2022 104468
- [25] S.M. Park, J.G. Jang, N.K. Lee, H.K. Lee, Physicochemical properties of binder gel in alkali-activated fly ash/slag exposed to high temperatures, Cement Concr. Res. 89 (2016) 72–79, https://doi.org/10.1016/j.cemconres.2016.08.004.
- [26] C.W. Bale, E. Bélisle, P. Chartrand, S.A. Decterov, G. Eriksson, K. Hack, I.-H. Jung, Y.-B. Kang, J. Melançon, A.D. Pelton, C. Robelin, S. Petersen, FactSage thermochemical software and databases recent developments, Calphad 33 (2009) 295–311, https://doi.org/10.1016/j.calphad.2008.09.009.
- [27] H. Xu, J.S.J. Van Deventer, The geopolymerisation of alumino-silicate minerals, Int. J. Miner. Process. 59 (2000) 247–266, https://doi.org/10.1016/S0301-7516 (99)00074-5.
- [28] S. Joseph, J. Skibsted, Ö. Cizer, A quantitative study of the C3A hydration, Cement Concr. Res. 115 (2019) 145–159, https://doi.org/10.1016/j. cemconres.2018.10.017.
- [29] M. Thiery, G. Villain, P. Dangla, G. Platret, Investigation of the carbonation front shape on cementitious materials: effects of the chemical kinetics, Cement Concr. Res. 37 (2007) 1047–1058, https://doi.org/10.1016/j.cemconres.2007.04.002.
- [30] A.F. Abdalqader, F. Jin, A. Al-Tabbaa, Characterisation of reactive magnesia and sodium carbonate-activated fly ash/slag paste blends, Constr. Build. Mater. 93 (2015) 506–513, https://doi.org/10.1016/j.conbuildmat.2015.06.015.

- [31] H. Rahier, B. Van Mele, J. Wastiels, Low-temperature synthesized aluminosilicate glasses, J. Mater. Sci. 31 (1996) 80–85, https://doi.org/10.1007/BF00355129.
- [32] J.G.S. Van Jaarsveld, J.S.J. Van Deventer, L. Lorenzen, The potential use of geopolymeric materials to immobilise toxic metals: Part I. Theory and applications, Miner. Eng. 10 (1997) 659–669, https://doi.org/10.1016/S0892-6875(97)00046-0
- [33] F. Qu, W. Li, Z. Tao, A. Castel, K. Wang, High temperature resistance of fly ash/ GGBFS-based geopolymer mortar with load-induced damage, Mater. Struct. 53 (2020) 111, https://doi.org/10.1617/s11527-020-01544-2.
- [34] P. Rovnaník, P. Bayer, P. Rovnaníková, Characterization of alkali activated slag paste after exposure to high temperatures, Constr. Build. Mater. 47 (2013) 1479–1487, https://doi.org/10.1016/j.conbuildmat.2013.06.070.
- [35] B. Mysen, P. Richet, Chapter 10 properties of iron-silicate glasses and melts, in: B. Mysen, P. Richet (Eds.), Silicate Glasses and Melts, second ed., Elsevier, 2019, pp. 349–402, https://doi.org/10.1016/B978-0-444-63708-6.00010-7.
- [36] O. Lila, G. Ameni, N.-A. Benoit, J. Jenny, B. Guillaume, D. Patrice, C. Clifford, G. Eric, S. Rossignol, Thermally resistant geopolymer to 1300 °C: scale-up and structural evolution, Open Ceramics 16 (2023) 100462, https://doi.org/10.1016/j. oceram.2023.100462.
- [37] M. Guerrieri, J.G. Sanjayan, Behavior of combined fly ash/slag-based geopolymers when exposed to high temperatures, Fire Mater. 34 (2010) 163–175, https://doi. org/10.1002/fam.1014.
- [38] X. Luo, W. Sun, S.Y.N. Chan, Effect of heating and cooling regimes on residual strength and microstructure of normal strength and high-performance concrete, Cement Concr. Res. 30 (2000) 379–383, https://doi.org/10.1016/S0008-8846(99) 00264-1